Graphical Abstract

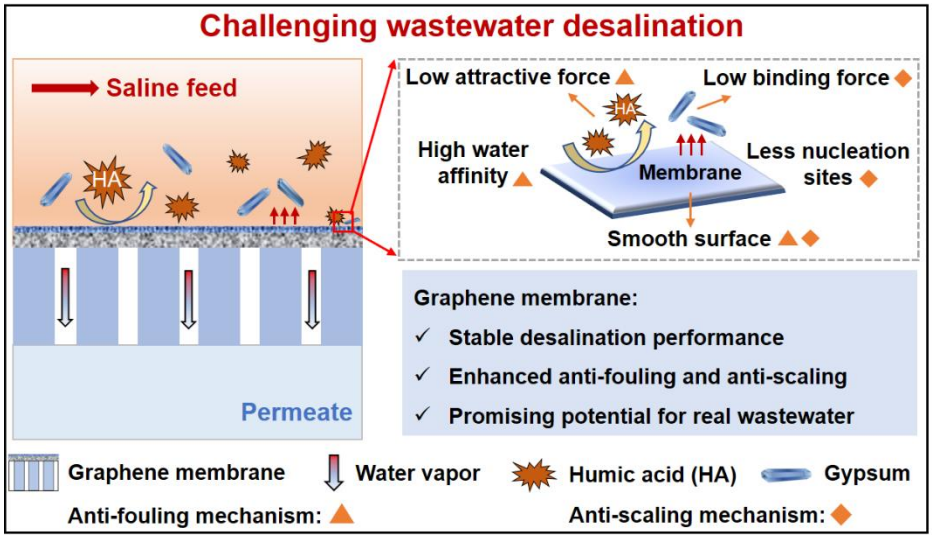

Robust ceramic-based graphene membrane for challenging water treatment with enhanced fouling and scaling resistance

Chunyi Sun[a], Bin Lin[c], Xiangyong Zheng[b], Yingchao Dong[a, b]*, Min Zhao[b]*, Chuyang Y. Tang[d]*

[a] Key Laboratory of Industrial Ecology and Environmental Engineering (Ministry of Education, MOE), School of Environmental Science and Technology, Dalian University of Technology, Dalian 116024, China

[b] College of Life and Environmental Science, Wenzhou University, Wenzhou 325035, China

[c] School of Mechanical and Electrical Engineering, University of Electronic Science and Technology of China, 611731 Chengdu, China

[d] Department of Civil Engineering, The University of Hong Kong, Pokfulam, Hong Kong, China

Abstract

Membrane fouling and scaling are two challenges for efficient treatment of hypersaline wastewater, greatly hindering separation performance and operation stability of desalination membranes. In this work, we report a smooth ceramic-based graphene desalination membrane, exhibiting enhanced anti-fouling and anti-scaling ability and operational performance for efficient treatment of both synthetic and real industrial wastewaters, outperforming polypropylene (PP) membrane. For treatment of hypersaline waters containing organic or inorganic substance, we demonstrate that the graphene membrane exhibits more stable water flux and almost complete salt rejection (>99.9%) during constant operation. Enhanced anti-fouling and desalination performance of graphene membrane could be attributed to the lower attractive interaction force with foulant (−4.65 mJ m^{-2}), lower surface roughness (R_a = 2.2 ± 0.1 nm) and higher affinity with water than PP membrane. Furthermore, an anti-scaling mechanism enabled by graphene membrane is evidenced, with a highlight on the roles of smooth graphene surface with lower roughness, less nucleation sites and lower binding force with scaling crystals. Importantly, even for industrial petrochemical wastewater, such a graphene membrane also exhibits relatively more stable water flux and promising oil and ions rejection during long-term operation, outperforming PP membrane. This study further confirms a promising practical application potential of robust ceramic-based graphene membrane for efficient treatment of more challenging hypersaline wastewater with complicated compositions, which is not feasible by conventional desalination membranes.

Keywords: Desalination; Hypersaline wastewater; Graphene membrane; Anti-fouling; Anti-scaling

1. Introduction

Water scarcity has become being one of the most urgent global challenges due to rapid population growth and severe water pollution (Dolan et al., 2021; Elimelech and Phillip 2011; Wang et al., 2020). Compared with conventional energy-intensive thermal methods, membrane-based desalination technologies featuring higher energy efficiency have attracted tremendous attention (Deshmukh et al., 2018; Lopez et al., 2023; Patel et al., 2020). Although reverse osmosis has been proven to be a gold standard desalination technology, it is not suitable for treating highly saline waters (>70 g L^{-1}) because of their ultrahigh osmotic pressure (Dong et al., 2022; Zuo et al., 2020). Recently, emerging thermal-membrane hybrid methods such as membrane distillation (MD) and pervaporation (PV) have been increasingly explored as competitive technologies for more challenging high-salinity wastewater treatment, e.g., for zero liquid discharge using low-grade thermal energy such as solar energy, geothermal energy and industrial waste heat (Farid et al., 2022; Lee et al., 2023; Li et al., 2021). However, current desalination membranes still suffer from some challenging issues such as membrane fouling, mineral scaling and pore wetting, especially over long-term operation (Liu et al., 2022; Wang et al., 2022a; Warsinger et al., 2015), which motivates us to develop reliable fouling/scaling mitigation strategies.

Hydrophobically modified polymeric membranes such as polypropylene (PP) has been developed since as early as 1960s due to their low cost and structural stability for membrane contactors and lab-scale desalination (Himma et al., 2016; Xu et al., 2017).

However, when treating more challenging hypersaline wastewater with complicated compositions, they often show high fouling/scaling/wetting propensity, low flux and deteriorated rejection (Ravi et al., 2020; Tibi et al., 2020). To address these limitations, tremendous efforts have recently been devoted to exploring rationally-designed anti-fouling or anti-scaling desalination membranes with specially engineered wettability, such as superhydrophobic membranes (Karanikola et al., 2018; Rezaei et al., 2018; Su et al., 2019), omniphobic membranes (Chang et al., 2020; Wang et al., 2019), and Janus composite membranes (Chen et al., 2021b; Feng et al., 2021). In spite of enhanced performance, most current modification strategies could only address one or some aspects of fouling, scaling and wetting issues. Due to complicated compositions in real industrial wastewater, membrane fouling, scaling and wetting usually occur simultaneously especially during long-term operation. It is necessary with practical significance to engineer new desalination membranes with simultaneous anti-fouling, anti-scaling and anti-wetting functions (Feng et al., 2022; Tong et al., 2023). Interestingly, atomically smooth graphene has attracted tremendous interests as an emerging desalination membrane owing to its specific surface and interfacial properties as well as suitable pore structure (Chen et al., 2021a; Liu et al., 2016). Rational design of robust graphene membranes would possibly provide a new platform that could simultaneously achieve promising anti-fouling/anti-scaling/anti-wetting and desalination performance for challenging hypersaline wastewater treatment.

Herein, unlike common modifications on MD membranes and processes, we

84 report a robust ceramic-based graphene desalination membrane with smooth surface for
85 more challenging desalination of hypersaline wastewater with complicated
86 compositions via PV process, enabling more promising resistance toward fouling,
87 scaling and wetting, which outperforms PP membrane–one of the dominant
88 desalination membranes. The fouling/scaling behavior and desalination performance of
89 both PP membrane and graphene membrane was systematically investigated for
90 treatment of synthetic hypersaline wastewater with the presence of humic acid (HA) or
91 gypsum ($CaSO_4$). More importantly, even for real industrial wastewater, the graphene
92 membrane also shows more promising performance and sustainable operation stability
93 than PP membrane. Detailed mechanistic insights are further provided to understand
94 the unique anti-fouling and anti-scaling process mechanism of graphene membrane via
95 both experimental and theoretical calculation results. In spite of two different
96 membrane processes, scientific understanding of enhanced anti-fouling/anti-scaling
97 mechanism is the main focus of our current work. In addition, such a comparison is
98 beneficial to select appropriate membrane and membrane process. Our study offers a
99 valuable reference toward rational design of robust desalination membrane
100 surface/interface with promising simultaneous anti-fouling and anti-scaling ability for
101 efficient treatment of more challenging hypersaline industrial wastewater.

102 **2. Materials and methods**

103 **2.1. Chemicals and materials**

104 Zirconia (ZrO_2, 3Y-TZP, 3 % mol yttrium oxide stabilized tetragonal zirconia

polycrystal) powder (Fanmeiya Materials Co., Ltd., China) was used as the raw material for preparation of ceramic substrate. Graphene oxide (GO) was purchased from Nanjing XFNANO Materials Tech. Co., Ltd., China. Chitosan (CS) was obtained from Sinopharm Chemical Reagent Co., Ltd., China. Sodium chloride (NaCl, AR), calcium chloride ($CaCl_2$, AR), sodium sulfate (Na_2SO_4, AR) and acetic acid (CH_3COOH, AR) were purchased from Damao Chemical Reagent Factory, China. Humic acid (HA) was supplied from Shanghai Aladdin Biochemical Technology Co., Ltd., China. The commercial PP membranes (Table S1 and Fig. S1) were purchased from Hangzhou Kaijie Membrane Separation Technology Co., Ltd., China. Both gases (argon and nitrogen, purity ≥ 99.999%) were obtained from Dalian Guanghui Gas Co., Ltd., China.

2.2. Membrane fabrication

The ZrO_2 ceramic substrates were prepared through a dry-wet spinning technology including immersion-induced phase inversion and dry-sintering process (Supporting Information S1.2, Fig. S2 and Fig. S3a–b). To fabricate the nanoporous γ-Al_2O_3 interlayer on ZrO_2 ceramic substrates (ZrO_2@γ-Al_2O_3) (Fig. S3c–d), a dip-coating method was employed with boehmite sol (Wang et al., 2022b). The GO solution (200 mg L^{-1}) was synthetized by adding GO power into deionized water, and then ultrasonicating for 3 h in a sonicator tank. The CS solution (0.4 wt.%) was prepared using acetic acid to ensure complete dissolution. 12.5 mL CS solution and 5 mL GO solution (200 mg L^{-1}) were dispersed in 50 mL deionized water. The mixtures were then placed onto a magnetic stirrer and vigorously stirred for 24 h to obtain homogeneous

GO-CS solution. The prepared GO-CS solution was vacuum-filtered using the circulating water multipurpose vacuum pump (SHZ-D (Ⅲ), Henan Yuhua Instrument Co., Ltd., China) for 20 min onto ZrO_2@γ-Al_2O_3 substrate by applying a vacuum of −0.097 MPa at the lumen side of the substrates (Fig. S4). The GO-CS membranes coated onto ZrO_2@γ-Al_2O_3 substrates were dried at room temperature overnight. Subsequently the membranes were placed into a tube furnace (OTF-1200X, Hefei Kejing Materials Technology Co., Ltd., China), heated at 200 °C for 2 h, and then annealed at 900 °C for 3 h in a flowing argon atmosphere (30 mL min^{-1}) to obtain the ceramic-based graphene membranes with most probable pore size of ~5.6 Å (Fig. S3e–f, Fig. S5, Table S2 and Fig. S6).

2.3. Membrane characterization

The microstructure and surface morphologies of PP membrane and graphene membrane were observed in a field emission scanning electron microscope (FE-SEM, NOVA NanoSEM 450, FEI company, USA) equipped with energy dispersive spectrometer (EDS) mapping analysis. The water contact angles of PP membrane and graphene membrane were measured by a dynamic contact angle goniometer (PT-705, Guangdong Zhongcheng Pussett Equipment Co., Ltd., China). Free-standing graphene membranes were prepared for N_2 adsorption and desorption analysis using an automatic physical adsorption instrument (AS-1-MP-11, Quantachrome, USA). Pore size distribution was determined by the Horvath-Kawazoe method (i.e., slit pore model). Raman spectra of GO-CS and graphene membranes were recorded in a Raman

147 spectrometer (inVia Qontor, Renishaw, UK). X-ray photoelectron spectroscopy (XPS,
148 Thermos K-Alpha+, USA) was employed to characterize the surface compositions of
149 GO-CS and graphene membranes. Atomic force microscopy (AFM, Dimension Icon,
150 Bruker, USA) was used to measure surface roughness of PP membrane and graphene
151 membrane. Three-dimensional excitation-emission matrix (3D-EEM) fluorescence
152 spectroscopy (F7100, Hitachi, Japan) was employed to quantify the fluorescent
153 compounds of industrial petrochemical wastewater and permeate. The feed and
154 permeate ion concentrations of industrial wastewater were measured by an inductively
155 coupled plasma optical emission spectrometer (ICP-OES, Avio 500, PerkinElmer,
156 USA). The tensile strength of commercial PP membrane and bending strength of
157 graphene membrane were tested in a universal testing machine (AGS-X, Shimadzu
158 (Suzhou) Instruments Manufacturing Co., Ltd., China). Detailed description of
159 experimental procedures can be found in Supporting Information S1.1 and S1.3.

160 **2.4. Performance test**

161 Desalination performance (water flux and salt rejection) of PP membrane and
162 graphene membrane was measured in a vacuum-assisted desalination setup (Fig. 1).
163 The fouling and scaling behavior of both PP membrane and graphene membrane was
164 systematically investigated for hypersaline water (NaCl, 70 g L^{-1}) containing different
165 concentrations of HA (10–40 mg L^{-1}) or gypsum ($CaSO_4$) (1–4 g L^{-1}) at 60 °C. Gypsum
166 solution was prepared by mixing $CaCl_2$ and $NaSO_4$ in deionized water without pH
167 adjustment. The real industrial petrochemical wastewater (secondary sedimentation
168 tank wastewater) was collected from Sinopec Shanghai Petrochemical Co., Ltd., China.

169 Oil concentrations of the feed and permeate for industrial petrochemical wastewater
170 were measured using an infrared oil detector (OIL460, Beijing China Invent Instrument
171 Technology Co., Ltd., China). A vacuum condition on the permeate side was maintained
172 at −0.097 MPa using a vacuum pump (2XZ-2, Linhai Tanshi Vacuum Equipment Co.,
173 Ltd., China) to drive the transport of water molecules across the membranes. A cold
174 trap cooled with liquid nitrogen was used to collect permeate for weighing at constant
175 time intervals. Water flux (J, L m^{-2} h^{-1}) and salt rejection (R, %) can be calculated by
176 the following equations (Si et al., 2020):

177 $$J = \frac{\Delta m}{A \rho \Delta t} \quad (1)$$

178 $$R = (1 - \frac{C_P}{C_f}) \quad (2)$$

179 where Δm (kg) is the mass of the permeate at a given time interval Δt (h), A (m^2) is the
180 effective area of the membrane, and ρ is the water density (0.9971 kg L^{-1}, 25 °C). The
181 salt concentrations (kg L^{-1}) of the feed (C_f) and permeate (C_p) were indirectly analyzed
182 using a conductivity meter (DDS-307A, INESA, Shanghai, China).

183 **2.5. Extended Derjaguin–Landau–Verwey–Overbeek (xDLVO) theory**

184 To better understand membrane fouling behavior and elucidate membrane fouling
185 mechanism, the xDLVO theory was used to calculate the interfacial interaction energies
186 between the organic foulant (HA) and membrane surfaces (PP or graphene). According
187 to the xDLVO theory, the total interfacial interaction energy between the foulant and
188 membrane surface immersed in water can be written as follows (Boo et al., 2018; Lin
189 et al., 2014):

190 $$\Delta G_{132}^{TOT} = \Delta G_{132}^{LW} + \Delta G_{132}^{AB} \quad (3)$$

where the subscripts 1, 2 and 3 denote the foulant, surface and water, respectively. The total interfacial interaction energy (ΔG_{132}^{TOT}) is obtained by summing the interaction energies from Lifshitz–van der Waals (LW) interaction (ΔG_{132}^{LW}) and acid–base (AB) interaction (ΔG_{132}^{AB}). The detailed calculation method and results are described in Supporting Information S2 (Tables S3–S6).

Fig. 1.

3. Results and discussion

3.1. Enhanced anti-fouling and desalination performance

Membrane fouling is a challenging issue in membrane-based desalination processes, where foulants accumulate on membrane surface and block membrane pore, usually resulting in the formation of a foulant layer and consequently performance decline (Boo et al. 2018; Horseman et al., 2020). As one of common natural organic matters, hydrophilic HA is considered as a major component of membrane fouling for MD desalination technology (Dong et al., 2018; Si et al. 2020). In this work, to address the key issue of HA fouling, we employed the specially-designed graphene membranes (via PV process) for desalination of challenging hypersaline water with presence of HA (Fig. 2), which outperformed PP membranes (via MD process). For both membranes, gradual decrease in water flux with increasing HA concentration could be ascribed to a decreased driving force with increased membrane fouling (Fig. 2a–c). Despite excellent

and stable salt rejection above 99.9% for both membranes, the graphene membrane exhibited much higher water flux than PP membrane at a wide range of HA concentrations (0–40 mg L^{-1}). Interestingly, even at a very high HA concentration (40 mg L^{-1}), the water flux of graphene membrane (20.3 ± 0.4 L m^{-2} h^{-1}) is still almost three times higher than that of PP membrane (7.1 ± 0.4 L m^{-2} h^{-1}), indicating a better desalination performance.

Specifically, in spite of maintaining a high and stable salt rejection (>99.8%), the PP membrane exhibits a rapid decrease in water flux (e.g., ~65% after a 100 h MD operation) due to severe membrane fouling (Fig. 2d–e), which could be reflected by a significantly decreased water contact angle from 106.0 ± 1.4° to 75.1 ± 1.0° after 100 h operation by the accumulation of more hydrophilic HA molecules (Fig. 2e inset). In contrast, besides promising salt rejection (>99.9%), the graphene membrane was able to maintain a relatively more stable water flux during 100 h operation (Fig. 2d), suggesting that better fouling resistance. It has a very low flux reduction rate (0.31% h^{-1}), when compared with those (0.33–7.30 % h^{-1}) of other state-of-the-art MD membranes (Table S7). This can be again verified by the SEM images of membrane surface with fouling mitigation, and more slightly decreased water contact angles before and after desalination operation (Fig. 2f).

Fig. 2.

3.2. Promising anti-scaling and desalination performance

In addition to membrane fouling, membrane scaling is the other important challenge for treatment of hypersaline water containing slightly soluble minerals such as sulfates (Horseman et al. 2020; Xiao et al., 2019b). Formation and accumulation of scaling precipitates on membrane surface usually lead to significant flux decline or severe membrane wetting (Karanikola et al. 2018; Xiao et al., 2019a). In our work, such an unfavorable phenomenon of $CaSO_4$ scaling was observed for conventional MD desalination membranes, especially PP membrane (Fig. 3a and Fig. 3c–e). In contrast, graphene membrane exhibited mitigated scaling and better desalination performance than PP membrane for treating hypersaline feed containing $CaSO_4$ (Fig. 3b–d and Fig. 3f). At a wide-range $CaSO_4$ concentration from 0 to 4 g L^{-1}, in spite of almost complete salt rejection (>99.9%) for both membranes, the water flux of graphene membrane is all higher than those of PP membranes. Especially, even at high $CaSO_4$ concentration (4 g L^{-1}), the graphene membrane still exhibited high water flux (20.5 ± 1.1 L m^{-2} h^{-1}), which is much higher (~3.3 times) than that of PP membrane with low water flux (6.3 ± 0.6 L m^{-2} h^{-1}).

In spite of constantly maintaining a high salt rejection (>99.8%) until ~70 h operation, the PP membrane shows rapid water flux decline (e.g., ~61% at ~70 h) (Fig. 3d). When further increasing operation time to 100 h, a significant decrease of salt rejection (~96.6%) was observed with high permeate conductivity (~3255.8 μS cm^{-1}) (Fig. S7), due to the occurrence of server scaling-induced pore wetting, which could be

fully confirmed by a significant change in surface morphologies and components (more $CaSO_4$ and NaCl scaling), and enhanced surface hydrophilicity (i.e., decreased water contact angles) (Fig. 3e and Fig. S8). In comparison, the graphene membrane displays an enhanced scaling/wetting resistance with relatively more stable water flux and nearly perfect salt rejection (>99.9%) during 100 h PV operation (Fig. 3d), indicating the better desalination performance. Moreover, it has a very low flux reduction rate (0.35% h^{-1}), which is lower than those (0.59–7.21 % h^{-1}) of reported polymeric membranes (Table S8). This conclusion can be also supported by the SEM images of membrane surface with mitigated membrane scaling (i.e., less $CaSO_4$ scaling and more stable water contact angles before and after desalination operation) (Fig. 3f and Fig. S9). In conclusion, these results clearly demonstrate that the graphene membrane has more promising anti-scaling and desalination performance.

Fig. 3.

3.3. Mechanistic insights into enhanced anti-fouling and anti-scaling

Understanding fouling mechanism is of great significance by probing membrane surface properties (e.g., hydrophobicity, roughness and pore size) (Du et al., 2018; Zuo et al., 2022). The pristine PP membrane shows a highly stable dynamic water contact angle (104.3°–107.7°) (Fig. 4a). But for the HA-fouled membrane, the water contact angle significantly decreased from 75.1° to 52.3° (~30.4% reduction) over time (180 s)

(Fig. 4a and Fig. 4c), which is attributed to the accumulation of more hydrophilic HA molecules. In contrast, both the pristine and HA-fouled graphene membranes fabricated in this work exhibited relatively low and constantly stable water contact angle (88.7°–91.9° for pristine membrane, and 76.4°–82.9° for HA-fouled membrane) (Fig. 4b and Fig. 4c), indicating the low organic fouling propensity. Compared with PP membrane, the surface of graphene membrane with enhanced hydrophilicity has higher affinity with water molecules, creating a more robust hydration layer that effectively resisted the deposition of hydrophilic organic foulants (Boo et al. 2018; Wang et al., 2016a; Wang et al., 2016b). In addition, the lower surface roughness and pore size of graphene membrane than PP membrane further decreases the contact area with foulants (Fig. 4d and Fig. 5a–c), resulting in a lower propensity for HA fouling. In PV, liquid water molecules transport across a dense selective polymeric or inorganic layer via solution-diffusion or adsorption-diffusion mechanism (Castro-Muñoz 2020; Wang et al. 2022b). In our work, the subnanometer pores (~5.6 Å) of graphene membranes play an important role in not only allowing the diffusion of small water molecules (2.8 Å) but also rejecting larger hydrated Na^+ (~7.2 Å) and Cl^- (~6.6 Å) ions. In this case, the selective graphene layer achieved high salt rejection. Unlike PV, in MD, the temperature difference between feed and permeate results in a partial vapor pressure difference that drives water vapor to transport through hydrophobic membrane pores (Si et al. 2020). Inside membrane pore, the transport of water vapor molecules is dominated by Knudsen diffusion, viscous flow, molecular diffusion or their combined

296 models (Sun et al., 2022).

297 In addition to surface properties, complicated interactions between membrane
298 surface and foulants also play a key role in membrane fouling (Ren et al., 2023). The
299 interfacial interaction energies between membrane surfaces (PP or graphene) and
300 foulants (HA) were calculated from interfacial forces based on xDLVO theory
301 (Supporting Information S2, Tables S3–S6) (Lin et al. 2014; Wang et al., 2013). The
302 interfacial force of HA–water was calculated to be –27.63 mN m^{-1} (Fig. 4e and Table
303 S5), suggesting its high affinity with water (i.e., high hydrophilicity). Compared with
304 PP membrane, the lower absolute values of interfacial forces (γ_{12}^{TOT} and γ_{23}^{TOT}) of
305 graphene membrane indicate its weaker affinity to foulants (HA) and stronger affinity
306 to water, which is more beneficial to form a hydration layer with less HA fouling on
307 graphene surface. More importantly, a much weaker interfacial attractive force for
308 graphene membrane (−4.65 mJ m^{-2}) was observed than PP membrane (−13.48 mJ m^{-2})
309 (Fig. 4f and Table S6), once again suggesting a lower organic fouling propensity. These
310 microscopic-level results correlate well with the above anti-fouling performance (Fig.
311 2). In summary, the anti-fouling mechanism for graphene membrane can be attributed
312 to the lower attractive interaction force, lower surface roughness and higher affinity
313 with water (Fig. 4g).

314

315 **Fig. 4.**

316

317 To understand the scaling process mechanisms of PP and graphene membranes,
318 we further studied their dynamic/static surface properties and compositions before and
319 after desalination operation. In spite of their both nominally flat and smooth surface
320 features at the macroscopic scale, the PP and graphene membrane surfaces have
321 obviously different nanoscale structures and morphologies (Fig. 5a–b). Specifically, the
322 average roughness value of PP membrane (R_a = 17.8 ± 3.8 nm) is almost one order of
323 magnitude higher than that of graphene membrane (R_a = 2.2 ± 0.1 nm) (Fig. 5c), which
324 is smoother with no visible crests or sags. The PP membrane with higher roughness not
325 only provided more heterogeneous nucleation sites, but also served as a cratered surface
326 for more facile growth and adhesion of scaling crystals. During the nucleation and
327 crystal growth stages, such a higher roughness further increased both the friction and
328 contact area between membrane surface and scaling crystals, resulting in an increased
329 probability of heterogeneous nucleation or crystal growth on membrane surface. Our
330 result is consistent with a prior study reporting that mineral crystallization became
331 severer with increasing surface roughness (Huang et al., 2020; Lin et al., 2011). In
332 contrast, the smooth graphene membrane surface had not only less heterogeneous
333 nucleation sites, but also notably lower binding force with scaling crystals (Zuo et al.
334 2022), resulting in a lower scaling propensity.
335 Such a mitigated membrane scaling can be also evidenced by the dynamic water
336 contact angle and SEM-EDS elemental mapping results (Fig. 5d–h). Different from the
337 scaled PP membrane with less stable water contact angle (Fig. 5d and Fig. 5f), the

graphene membranes before and after operation both show more stable dynamic water contact angle (88.7°–91.9° before operation, and 74.1°–86.1° after operation) (Fig. 5e–f), indicating the low mineral scaling propensity. Moreover, unlike PP membrane surface with more Ca and Na elements (Fig. 5g and Fig. S8), the graphene membrane has much less Ca and Na elements detected after desalination operation, and no observable crystals accumulated on the surface (Fig. 5h and Fig. S9). These observations indicate that graphene membrane has some unique advantages to resist mineral scaling, outperforming PP membrane. In addition, scaling crystals are likely produced via a nonclassical nucleation process where the aggregation of precursor clusters and their interactions with membrane surface regulate the formation of heterogeneous scale (Tong et al. 2023; Yin et al., 2022). In this case, graphene membrane surface with enhanced hydrophilicity is more favorable for reducing surface scaling propensity due to their lower affinity with precursor clusters and higher affinity with water. Such a mechanism is analogous to that behind using hydrophilic surfaces to achieve enhanced organic fouling resistance (Fig. 4). In summary, the anti-scaling mechanism of graphene membrane can be attributed to its smooth surface with lower roughness, less nucleation sites, lower binding force with scaling crystals, and higher affinity with water (Fig. 5i).

Fig. 5.

3.4. Promising application potential for industrial wastewater treatment

Unlike synthetic high-salinity water, efficient treatment of real wastewater is more challenging due to its complicated components. To further evaluate the feasibility for practical application, we tested the desalination performance for treatment of industrial petrochemical wastewater (Fig. 6a) using PP membrane and graphene membrane. In this work, the feed wastewater contains oily emulsion (total oil, 26.30 mg L^{-1}) and inorganic salts such as Na^+, Ca^{2+}, Mg^{2+}, K^+ (total conductivity ~3.9 mS cm^{-1}) (Table S9). For PP membrane, a rapid decrease was observed for both salt rejection (from 97.4 to 82.1%) and water flux (from 9.5 to 1.2 L m^{-2} h^{-1}) during only 32 h MD operation, indicating a failure of MD desalination capacity by pore-wetting and membrane fouling (Fig. 6b and Fig. S10). The SEM images and decreased water contact angles further confirm severe membrane fouling/scaling of PP membrane after MD operation (Fig. 6d). In addition, commercial polytetrafluoroethylene (PTFE) membrane also exhibits significant decrease in water flux (from 7.0 to 1.9 L m^{-2} h^{-1}) and salt rejection (from 99.1 to 84.3%) after 50 h operation (Fig. S11), due to the severe fouling, scaling and wetting (Fig. S12). Different from commercial PP and PTFE membranes with rapid flux decrease, the graphene membrane shows relatively more stable water flux during constant PV operation (until 100 h), despite a gradual decrease due to the inevitable fouling/scaling caused by the complicated compositions of feed wastewater. The flux reduction rate (0.60 % h^{-1}) of graphene membrane was much lower (i.e., ~5 times lower) than that (2.69 % h^{-1}) of PP membrane (Fig. 6c and Table S10). More importantly, the

graphene membrane also exhibits much more constantly stable salt rejection (~98.8%) and low permeate conductivity (~47.5 μS cm^{-1}) until 100 h (Fig. 6b and Fig. S10). Such a mitigated membrane fouling/scaling can be also supported by the accumulation of less foulants on membrane surface with more stable water contact angles before and after operation (Fig. 6e). Moreover, the presence of less multiple elements (e.g., O, N, S, Cl, K, Ca) further shows that less fouling/scaling was formed on graphene membrane than PP membrane (Table S11).

Moreover, 3D-EEM fluorescence spectra were collected to further analyze the rejection of organic components in feed and permeate for both membranes (Fig. 6f–g and Fig. S13). The feed of petrochemical wastewater contains various chemical compounds such as tryptophan-like substances (II), fulvic acid-like substances (III), soluble microbial byproduct substances (IV) and humic acid-like substances (V) (Fig. 6f and Table S12) (Chen et al., 2003; Song et al., 2020). Unlike PP membrane (with organic residues in the permeate, Fig. S13), the graphene membrane was able to completely reject the organic components, which were not identified in the regions II, III, IV and V (Fig. 6g). Moreover, the graphene membrane also exhibited the better rejection of oil and inorganic ions (e.g., Na^+, Ca^{2+}, Mg^{2+} and K^+) than PP membrane (Fig. 6h and Table S9). In addition, after efficient treatment by using graphene membrane, all the ionic concentrations of the permeate are lower than the World Health Organization (WHO) drinking water standard (Edition 2011). The promising separation performance and operational stability of graphene membrane demonstrate a good

401 practical application potential of efficiently treating industrial wastewater.

402 For the treatment of synthetic and real wastewaters, the graphene membrane
403 exhibited better anti-fouling and anti-scaling performance than more hydrophobic
404 commercial polymeric membranes such as PP membranes. In addition to surface
405 wetting, other mechanism factors such as interaction force, nucleation site and
406 roughness are responsible for mitigating membrane fouling and scaling. Enhanced anti-
407 fouling performance could be attributed to the lower attractive interaction force with
408 foulant, lower surface roughness and higher affinity with water while enhanced anti-
409 scaling could be ascribed to lower roughness surface, less nucleation sites and lower
410 binding force with scaling crystals. Nevertheless, the fabricated graphene membrane
411 indeed suffered from progressively enhanced fouling and scaling with time (i.e.,
412 gradual flux decline) during long-term single-cycle operation (Fig. 6b). Future research
413 is still highly needed by developing more e□ective surface-modification or
414 pretreatment strategies to further mitigate fouling and scaling to improve desalination
415 performance.

416

417 **Fig. 6.**

418

419 **4. Conclusions**

420 Treatment of more challenging hypersaline wastewater is of practical significance
421 for membrane technology. In this study, we demonstrate the promising performance

422 and unique anti-fouling and anti-scaling process mechanism of ceramic-based graphene
423 membrane for efficient treatment of both synthetic and real industrial wastewaters with
424 complicated compositions, which can be considered as a more promising alternative to
425 commercial PP membrane. For treatment of organic hypersaline water, the graphene
426 membrane was able to maintain not only promising salt rejection (all >99.9%), but also
427 more stable water flux than PP membrane during constant operation due to its mitigated
428 organic fouling. Such mitigated organic fouling could be attributed to the lower surface
429 roughness (R_a = 2.2 ± 0.1 nm), lower attractive interaction force with foulant (−4.65 mJ
430 m^{-2}), and higher surface affinity with water molecules for graphene membrane than PP
431 membrane. Moreover, for treatment of hypersaline water containing inorganic gypsum,
432 the graphene membrane displays a relatively more stable water flux, and especially
433 more highly stable salt rejection (>99.9%) during operation than PP membrane, which
434 suffers from lower salt rejection due to the severe scaling and wetting issues. The
435 enhanced scaling/wetting resistance of graphene membrane can be ascribed to its
436 specific surface and interfacial properties such as smooth graphene surface with lower
437 roughness, less nucleation sites and lower binding force with scaling crystals. More
438 importantly, even for industrial petrochemical wastewater, the graphene membrane also
439 shows not only more promising performance (such as higher water flux and higher
440 rejections for inorganic salt ions and total oil), but also better and more sustainable
441 long-term operation stability, outperforming PP membrane. Therefore, the performance
442 enhancement strategy through achieving simultaneous anti-fouling and anti-scaling

443 ability will not only provide a valuable reference for rationally designing robust
444 desalination membranes with specific surface and structure properties, enabling more
445 challenging water treatment applications, which could not be well performed by
446 conventional technologies.

447 Besides the lab-scale membrane configuration designed in this work, it is
448 challenging that graphene membranes should be massively produced into larger tubular
449 or flat-sheet dimensions for large-scale application using reliable manufacturing
450 techniques such as extrusion-sintering, dip-coating and vacuum-filtration processes. In
451 spite of two different membrane processes, scientific understanding of enhanced anti-
452 fouling/anti-scaling mechanism is the main focus of our current work via both
453 experimental and theoretical calculation results. The aim of such a comparison is to
454 select appropriate membrane and membrane process. Energy consumption calculation
455 for desalination process is a complicated process. In the following work, energy
456 consumption will be calculated and compared for these two processes based on
457 experimental and model simulation methods. Most conventional processes with a bulk
458 heating mode are energy intensive, which needs to be fully addressed to decrease energy
459 consumption. Considering the promising photothermal or electrothermal properties of
460 graphene, an interfacial heating enhanced protocol will be also employed in our
461 following work to further not only enhance desalination performance by significantly
462 mitigating scaling and fouling, but also decrease energy consumption, which are still
463 less concerned for current studies. In addition, more robust ceramic-based graphene

membranes are also expected to have promising applications in chemically or physically harsh environments.

Acknowledgements

This work was financially supported by the NSFC-RGC Joint Program (No. 52261160381) and NSFC General Program (No. 52070033) of National Natural Science Foundation of China. CY Tang is supported by a research project founded by the Research Grants Council of Hong Kong (N_HKU721/22).

References

Boo, C., Hong, S., Elimelech, M., 2018. Relating organic fouling in membrane distillation to intermolecular adhesion forces and interfacial surface energies. Environ. Sci. Technol. 52 (24), 14198–14207.

Castro-Muñoz, R., 2020. Breakthroughs on tailoring pervaporation membranes for water desalination: a review. Water Res. 187, 116428.

Chang, H., Liu, B., Zhang, Z., Pawar, R., Yan, Z., Crittenden, J.C., Vidic, R.D., 2020. A critical review of membrane wettability in membrane distillation from the perspective of interfacial interactions. Environ. Sci. Technol. 55 (3), 1395–1418.

Chen, W., Westerhoff, P., Leenheer, J.A., Booksh, K., 2003. Fluorescence excitation− emission matrix regional integration to quantify spectra for dissolved organic matter. Environ. Sci. Technol. 37 (24), 5701–5710.

Chen, X., Zhu, Y.-B., Yu, H., Liu, J.Z., Easton, C.D., Wang, Z., Hu, Y., Xie, Z., Wu, H.-A., Zhang, X., 2021a. Ultrafast water evaporation through graphene membranes with subnanometer pores for desalination. J. Membr. Sci. 621, 118934.

Chen, Y., Lu, K.-J., Gai, W., Chung, T.-S., 2021b. Nanofiltration-inspired Janus membranes with simultaneous wetting and fouling resistance for membrane

489 distillation. Environ. Sci. Technol. 55 (11), 7654–7664.
490 Deshmukh, A., Boo, C., Karanikola, V., Lin, S., Straub, A.P., Tong, T., Warsinger, D.M.,
491 Elimelech, M., 2018. Membrane distillation at the water-energy nexus: limits,
492 opportunities, and challenges. Energy Environ. Sci. 11 (5), 1177–1196.
493 Dolan, F., Lamontagne, J., Link, R., Hejazi, M., Reed, P., Edmonds, J., 2021. Evaluating
494 the economic impact of water scarcity in a changing world. Nat. Commun. 12 (1),
495 1915.
496 Dong, Y., Ma, L., Tang, C.Y., Yang, F., Quan, X., Jassby, D., Zaworotko, M.J., Guiver,
497 M.D., 2018. Stable superhydrophobic ceramic-based carbon nanotube composite
498 desalination membranes. Nano Lett. 18 (9), 5514–5521.
499 Dong, Y., Wu, H., Yang, F., Gray, S., 2022. Cost and efficiency perspectives of ceramic
500 membranes for water treatment. Water Res. 220, 118629.
501 Du, X., Zhang, Z., Carlson, K.H., Lee, J., Tong, T., 2018. Membrane fouling and
502 reusability in membrane distillation of shale oil and gas produced water: effects of
503 membrane surface wettability. J. Membr. Sci. 567, 199–208.
504 Edition, F., 2011. Guidelines for drinking-water quality. WHO Chron. 38 (4), 104–108.
505 Elimelech, M., Phillip, W.A., 2011. The future of seawater desalination: energy,
506 technology, and the environment. Science 333 (6043), 712–717.
507 Farid, M.U., Kharraz, J.A., Lee, C.-H., Fang, J.K.-H., St-Hilaire, S., An, A.K., 2022.
508 Nanobubble-assisted scaling inhibition in membrane distillation for the treatment
509 of high-salinity brine. Water Res. 209, 117954.
510 Feng, D., Chen, Y., Wang, Z., Lin, S., 2021. Janus membrane with a dense hydrophilic
511 surface layer for robust fouling and wetting resistance in membrane distillation:
512 new insights into wetting resistance. Environ. Sci. Technol. 55 (20), 14156–14164.
513 Feng, D., Li, X., Wang, Z., 2022. Comparison of omniphobic membranes and Janus
514 membranes with a dense hydrophilic surface layer for robust membrane
515 distillation. J. Membr. Sci. 660, 120858.
516 Himma, N.F., Anisah, S., Prasetya, N., Wenten, I.G., 2016. Advances in preparation,

517 modification, and application of polypropylene membrane. J. Polym. Eng. 36 (4),
518 329–362.
519 Horseman, T., Yin, Y., Christie, K.S., Wang, Z., Tong, T., Lin, S., 2020. Wetting, scaling,
520 and fouling in membrane distillation: state-of-the-art insights on fundamental
521 mechanisms and mitigation strategies. ACS ES&T Eng. 1 (1), 117–140.
522 Huang, X., Li, C., Zuo, K., Li, Q., 2020. Predominant effect of material surface
523 hydrophobicity on gypsum scale formation. Environ. Sci. Technol. 54 (23),
524 15395–15404.
525 Karanikola, V., Boo, C., Rolf, J., Elimelech, M., 2018. Engineered slippery surface to
526 mitigate gypsum scaling in membrane distillation for treatment of hypersaline
527 industrial wastewaters. Environ. Sci. Technol. 52 (24), 14362–14370.
528 Lee, B., Wang, L., Wang, Z., Cooper, N.J., Elimelech, M., 2023. Directing the research
529 agenda on water and energy technologies with process and economic analysis.
530 Energy Environ. Sci. 16, 714–722.
531 Li, H., Fu, M., Wang, S.-Q., Zheng, X., Zhao, M., Yang, F., Tang, C.Y., Dong, Y., 2021.
532 Stable Zr-based metal–organic framework nanoporous membrane for efficient
533 desalination of hypersaline water. Environ. Sci. Technol. 55 (21), 14917–14927.
534 Lin, N.H., Shih, W.-Y., Lyster, E., Cohen, Y., 2011. Crystallization of calcium sulfate
535 on polymeric surfaces. J. Colloid Interf. Sci. 356 (2), 790–797.
536 Lin, T., Shen, B., Chen, W., Zhang, X., 2014. Interaction mechanisms associated with
537 organic colloid fouling of ultrafiltration membrane in a drinking water treatment
538 system. Desalination 332 (1), 100–108.
539 Liu, G., Jin, W., Xu, N., 2016. Two□dimensional□material membranes: a new family
540 of high□performance separation membranes. Angew. Chem. Int. Ed. 55 (43),
541 13384–13397.
542 Liu, J., Wang, Y., Li, S., Li, Z., Liu, X., Li, W., 2022. Insights into the wetting
543 phenomenon induced by scaling of calcium sulfate in membrane distillation. Water
544 Res. 216, 118282.

545 Lopez, K.P., Wang, R., Hjelvik, E.A., Lin, S., Straub, A.P., 2023. Toward a universal
546 framework for evaluating transport resistances and driving forces in membrane-
547 based desalination processes. Sci. Adv. 9 (1), eade0413.
548 Patel, S.K., Ritt, C.L., Deshmukh, A., Wang, Z., Qin, M., Epsztein, R., Elimelech, M.,
549 2020. The relative insignificance of advanced materials in enhancing the energy
550 efficiency of desalination technologies. Energy Environ. Sci. 13 (6), 1694–1710.
551 Ravi, J., Othman, M.H.D., Matsuura, T., Bilad, M.R.i., El-Badawy, T., Aziz, F., Ismail,
552 A., Rahman, M.A., Jaafar, J., 2020. Polymeric membranes for desalination using
553 membrane distillation: a review. Desalination 490, 114530.
554 Ren, L.-F., Li, J., Xu, Y., Shao, J., He, Y., 2023. Novel sandwich-like membrane with
555 hydrophilic-omniphobic-hydrophilic structure for sustainable water recovery in
556 membrane distillation. Resour. Conserv. Recy. 188, 106646.
557 Rezaei, M., Warsinger, D.M., Duke, M.C., Matsuura, T., Samhaber, W.M., 2018.
558 Wetting phenomena in membrane distillation: mechanisms, reversal, and
559 prevention. Water Res. 139, 329–352.
560 Si, Y., Sun, C., Li, D., Yang, F., Tang, C.Y., Quan, X., Dong, Y., Guiver, M.D., 2020.
561 Flexible superhydrophobic metal-based carbon nanotube membrane for
562 electrochemically enhanced water treatment. Environ. Sci. Technol. 54 (14),
563 9074–9082.
564 Song, C., Qi, D., Han, Y., Xu, Y., Xu, H., You, S., Wang, W., Wang, C., Wei, Y., Ma, J.,
565 2020. Volatile-organic-compound-intercepting solar distillation enabled by a
566 photothermal/photocatalytic nanofibrous membrane with dual-scale pores.
567 Environ. Sci. Technol. 54 (14), 9025–9033.
568 Su, C., Horseman, T., Cao, H., Christie, K., Li, Y., Lin, S., 2019. Robust
569 superhydrophobic membrane for membrane distillation with excellent scaling
570 resistance. Environ. Sci. Technol. 53 (20), 11801–11809.
571 Sun, C., Lyu, Q., Si, Y., Tong, T., Lin, L.-C., Yang, F., Tang, C.Y., Dong, Y., 2022.
572 Superhydrophobic carbon nanotube network membranes for membrane

573 distillation: high-throughput performance and transport mechanism. Environ. Sci.
574 Technol. 56 (9), 5775–5785.
575 Tibi, F., Charfi, A., Cho, J., Kim, J., 2020. Fabrication of polymeric membranes for
576 membrane distillation process and application for wastewater treatment: critical
577 review. Process Saf. Environ. Prot. 141, 190–201.
578 Tong, T., Liu, X., Li, T., Park, S., Anger, B., 2023. A tale of two foulants: the coupling
579 of organic fouling and mineral scaling in membrane desalination. Environ. Sci.
580 Technol. 57 (18), 7129–7149.
581 Wang, P., Cheng, W., Zhang, X., Liu, Q., Li, J., Ma, J., Zhang, T., 2022a. Membrane
582 scaling and wetting in membrane distillation: mitigation roles played by humic
583 substances. Environ. Sci. Technol. 56 (5), 3258–3266.
584 Wang, Q., Wang, Z., Zhu, C., Mei, X., Wu, Z., 2013. Assessment of SMP fouling by
585 foulant–membrane interaction energy analysis. J. Membr. Sci. 446, 154–163.
586 Wang, W., Du, X., Vahabi, H., Zhao, S., Yin, Y., Kota, A.K., Tong, T., 2019. Trade-off
587 in membrane distillation with monolithic omniphobic membranes. Nat. Commun.
588 10 (1), 1–9.
589 Wang, X., Li, Y., Yu, H., Yang, F., Tang, C.Y., Quan, X., Dong, Y., 2020. High-flux
590 robust ceramic membranes functionally decorated with nano-catalyst for emerging
591 micro-pollutant removal from water. J. Membr. Sci. 611, 118281.
592 Wang, X., Lyu, Q., Tong, T., Sun, K., Lin, L.-C., Tang, C.Y., Yang, F., Guiver, M.D.,
593 Quan, X., Dong, Y., 2022b. Robust ultrathin nanoporous MOF membrane with
594 intra-crystalline defects for fast water transport. Nat. Commun. 13 (1), 1–11.
595 Wang, Z., Hou, D., Lin, S., 2016a. Composite membrane with underwater-oleophobic
596 surface for anti-oil-fouling membrane distillation. Environ. Sci. Technol. 50 (7),
597 3866–3874.
598 Wang, Z., Jin, J., Hou, D., Lin, S., 2016b. Tailoring surface charge and wetting property
599 for robust oil-fouling mitigation in membrane distillation. J. Membr. Sci. 516,
600 113–122.

601 Warsinger, D.M., Swaminathan, J., Guillen-Burrieza, E., Arafat, H.A., 2015. Scaling
602 and fouling in membrane distillation for desalination applications: a review.
603 Desalination 356, 294–313.
604 Xiao, Z., Li, Z., Guo, H., Liu, Y., Wang, Y., Yin, H., Li, X., Song, J., Nghiem, L.D., He,
605 T., 2019a. Scaling mitigation in membrane distillation: from superhydrophobic to
606 slippery. Desalination 466, 36–43.
607 Xiao, Z., Zheng, R., Liu, Y., He, H., Yuan, X., Ji, Y., Li, D., Yin, H., Zhang, Y., Li, X.-
608 M., 2019b. Slippery for scaling resistance in membrane distillation: a novel porous
609 micropillared superhydrophobic surface. Water Res. 155, 152–161.
610 Xu, Z., Liu, Z., Song, P., Xiao, C., 2017. Fabrication of super-hydrophobic
611 polypropylene hollow fiber membrane and its application in membrane distillation.
612 Desalination 414, 10–17.
613 Yin, Y., Li, T., Zuo, K., Liu, X., Lin, S., Yao, Y., Tong, T., 2022. Which surface is more
614 scaling resistant? A closer look at nucleation theories for heterogeneous gypsum
615 nucleation in aqueous solutions. Environ. Sci. Technol. 56 (22), 16315–16324.
616 Zuo, K., Wang, W., Deshmukh, A., Jia, S., Guo, H., Xin, R., Elimelech, M., Ajayan,
617 P.M., Lou, J., Li, Q., 2020. Multifunctional nanocoated membranes for high-rate
618 electrothermal desalination of hypersaline waters. Nat. Nanotechnol. 15 (12),
619 1025–1032.
620 Zuo, K., Zhang, X., Huang, X., Oliveira, E.F., Guo, H., Zhai, T., Wang, W., Alvarez,
621 P.J., Elimelech, M., Ajayan, P.M., 2022. Ultrahigh resistance of hexagonal boron
622 nitride to mineral scale formation. Nat. Commun. 13 (1), 4523.
623

Figure

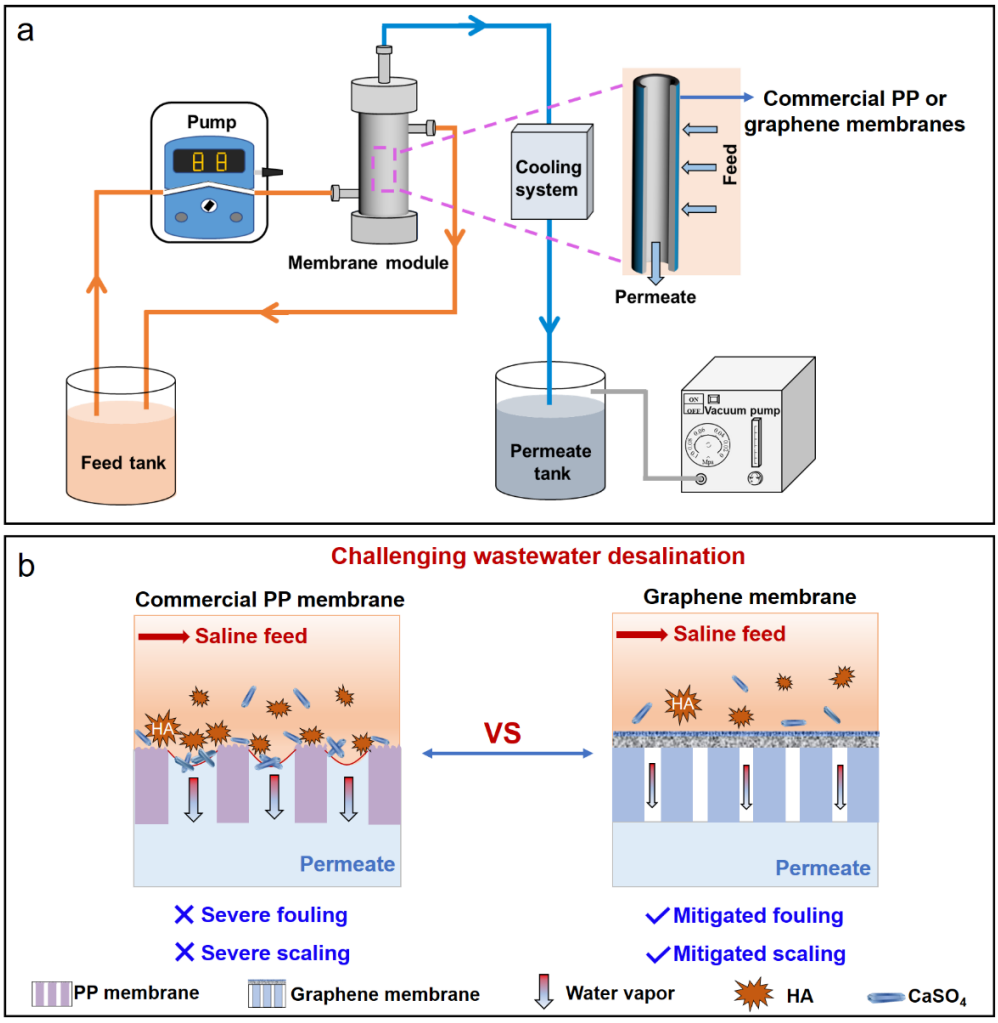

Fig. 1. (a) Schematic diagram of the vacuum-assisted desalination setup. (b) Schematic diagram of desalination membrane processes for polypropylene (PP) membrane (via membrane distillation process) and graphene membrane (via pervaporation process, fabricated in this work) for treatment of challenging hypersaline waters containing humic acid (HA) or gypsum ($CaSO_4$).

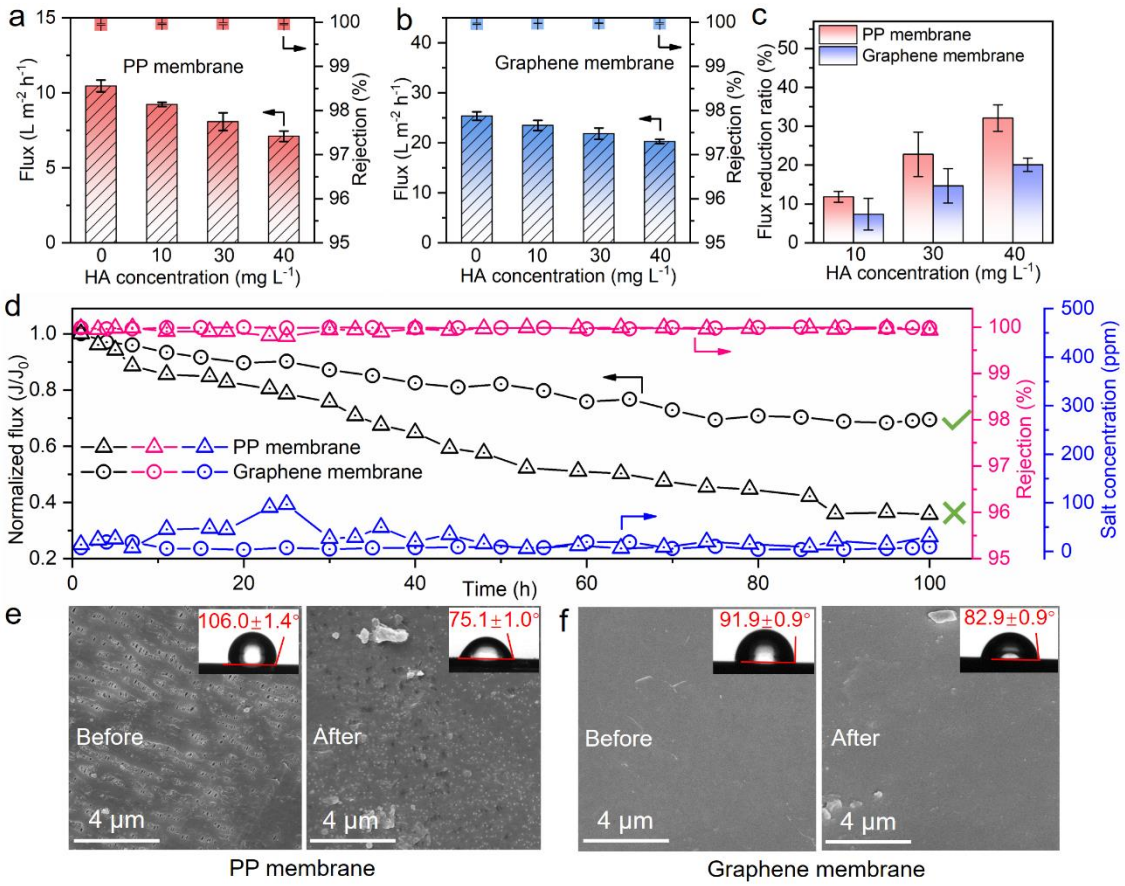

Fig. 2. Desalination performance and fouling of PP membrane and graphene membrane for treatment of hypersaline water (70 g L^{-1} NaCl) with presence of HA (0–40 mg L^{-1}) at 60 °C. Desalination performance (water flux and rejection) of (a) PP membrane and (b) graphene membrane for treatment of hypersaline water containing different HA concentrations ranging from 0 to 40 mg L^{-1}. (c) Flux reduction ratio of PP membrane and graphene membrane for treatment of hypersaline water containing HA (10–40 mg L^{-1}). (d) Comparison of desalination performance (normalized water flux and salt rejection) between PP membrane and graphene membrane for treatment of hypersaline water with presence of HA (40 mg L^{-1}). Membrane surface SEM images and water contact angles in air (inset) of (e) PP membrane and (f) graphene membrane before and after desalination operation (feed solution: 40 mg L^{-1} HA, 70 g L^{-1} NaCl).

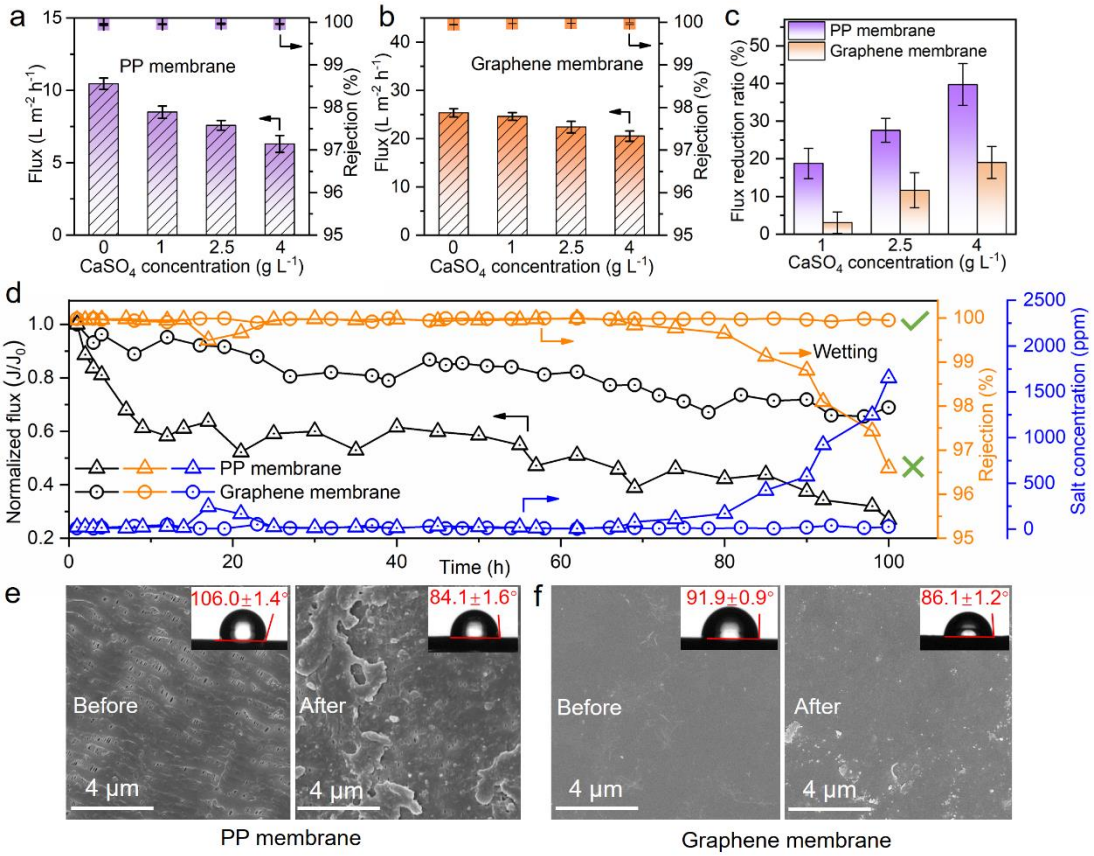

Fig. 3. Desalination performance of PP and graphene membranes for treatment of hypersaline water (70 g L^{-1} NaCl) with presence of $CaSO_4$ (0–4 g L^{-1}) at 60 °C. Desalination performance (water flux and rejection) of (a) PP membrane and (b) graphene membrane for treatment of hypersaline water containing different $CaSO_4$ concentrations ranging from 0 to 4 g L^{-1}. (c) Flux reduction ratio of PP membrane and graphene membrane for treatment of hypersaline water containing $CaSO_4$ (1–4 g L^{-1}). (d) Comparison of desalination performance (normalized water flux and salt rejection) between PP membrane and graphene membrane for treatment of hypersaline water with presence of $CaSO_4$ (4 g L^{-1}). Membrane surface SEM images and water contact angles in air (inset) of (e) PP membrane and (f) graphene membrane before and after desalination operation (feed solution: 4 g L^{-1} $CaSO_4$, 70 g L^{-1} NaCl).

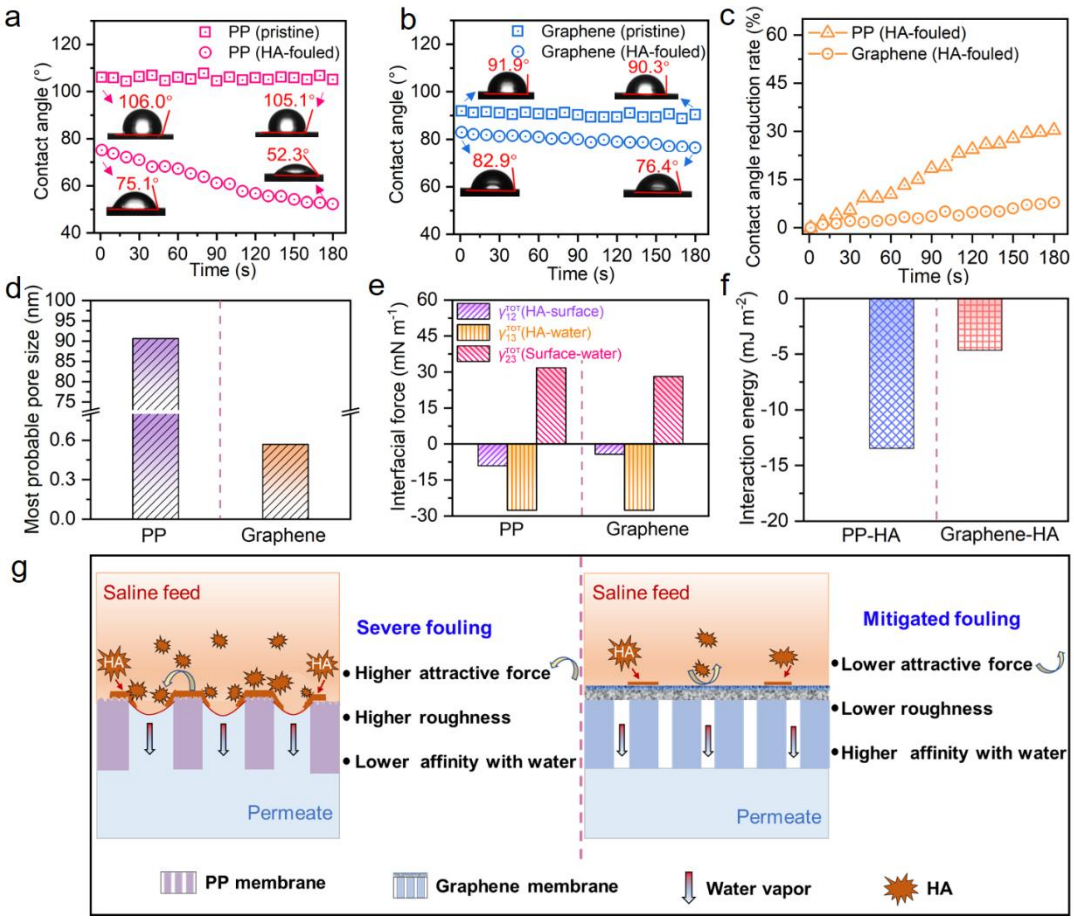

Fig. 4. Surface properties and interaction energies of PP membrane and graphene membrane. Dynamic water contact angle over time (180 s) of (a) PP membrane and (b) graphene membrane before and after desalination operation for treatment of hypersaline water (70 g L^{-1} NaCl) containing HA (40 mg L^{-1}). (c) Dynamic water contact angle reduction rate over time of PP membrane (HA-fouled) and graphene membrane (HA-fouled) after desalination operation. (d) Most probable pore size (nm) of PP membrane and graphene membrane. (e) Interfacial forces (mN m^{-1}) between foulant (HA)–surface (γ_{12}^{TOT}), foulant (HA)–water (γ_{13}^{TOT}) and surface–water (γ_{23}^{TOT}) (the subscripts 1, 2 and 3 donate foulant, membrane surface and water, respectively). (f) Interfacial interaction energies (ΔG_{132}^{TOT}, mJ m^{-2}) between the foulant (HA) and membrane surface. (g) Schematic illustration of fouling process mechanisms for fouling-prone PP membrane (left) and fouling-resistant graphene membrane (right).

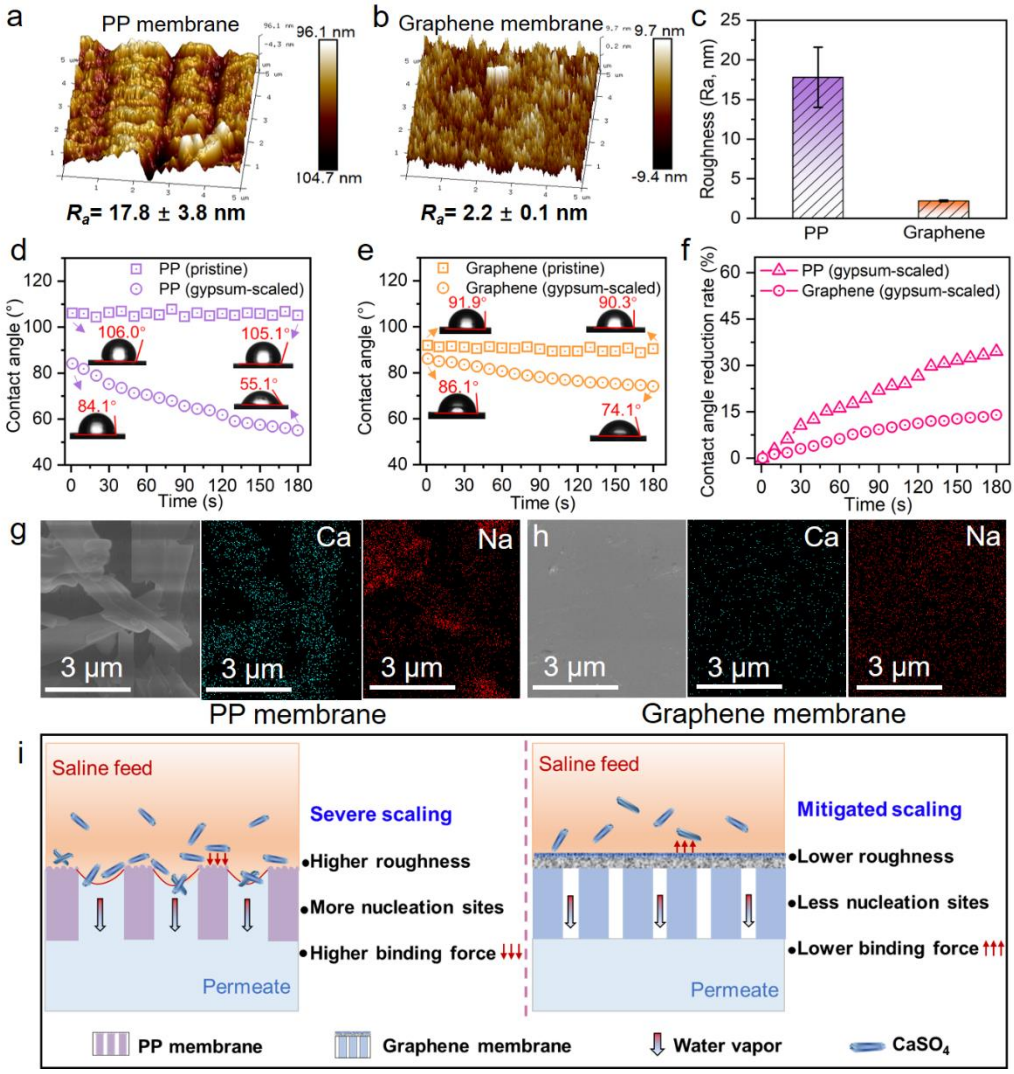

Fig. 5. Surface properties and scaling mechanism of PP membrane and graphene membrane. AFM images of (a) PP membrane and (b) graphene membrane. (c) Surface roughness comparison of PP membrane and graphene membrane. Dynamic water contact angle over time (180 s) of (d) PP membrane and (e) graphene membrane before (pristine) and after (gypsum-scaled) desalination operation for treatment of hypersaline water (70 g L^{-1} NaCl) containing $CaSO_4$ (4 g L^{-1}). (f) Dynamic water contact angle reduction rate over time of PP membrane (gypsum-scaled) and graphene membrane (gypsum-scaled) after desalination operation. SEM images and EDS element mapping images (cyan: Ca; red: Na) of the outer surface of (g) PP membrane and (h) graphene membrane after 100-h desalination operation (70 g L^{-1} NaCl, 4 g L^{-1} $CaSO_4$). (i) Schematic illustration of scaling process mechanisms for scaling-prone PP membrane (left) and scaling-mitigated graphene membrane (right).

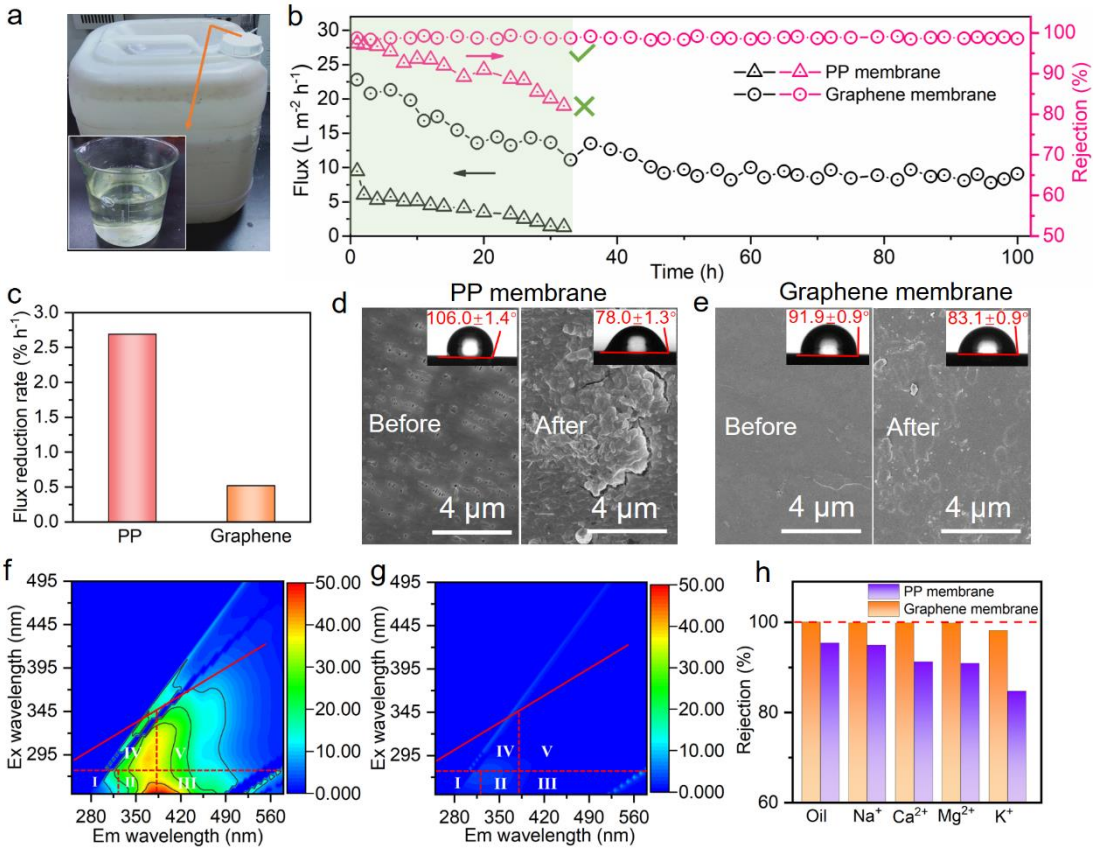

Fig. 6. Performance, fouling and scaling of PP membrane and graphene membrane for treatment of real industrial petrochemical wastewater. (a) Photos of industrial petrochemical wastewater. (b) Desalination performance (water flux and rejection) of PP membrane and graphene membrane (operation temperature: 60 °C). (c) Comparison of flux reduction ratio between PP membrane and graphene membrane. Membrane surface SEM images and water contact angles in air (inset) of (d) PP membrane and (e) graphene membrane before and after separation operation (feed: industrial petrochemical wastewater). 3D-EEM fluorescence spectra of (f) industrial petrochemical wastewater and (g) permeate using graphene membrane. (h) Rejection comparison of PP membrane and graphene membrane.

Electronic Supplementary Material (for online publication only)

Supporting Information.pdf